RSC Advances

ROYAL SOCIETY OF CHEMISTRY

www.rsc.org/advances

Gold nanoparticles modified graphitic carbon nitride/multi-walled carbon nanotubes (g-C_3N_4/CNTs/Au) hybrid photocatalysts for effective water splitting and degradation

Rajendra C. Pawar[1], Suhee Kang[1], Sung Hoon Ahn[2] and Caroline Sunyong Lee[1]*

[1]Department of Materials Engineering, Hanyang University,

Ansan 426-791, Gyeonggi-do, South Korea

[2]School of Mechanical & Aerospace Engineering, Seoul National University,

Seoul 151-742, South Korea

ABSTRACT

Gold nanoparticles (Au) used for stable plasmonic photocatalysts in hybrids of Au, graphitic carbon nitride (g-C_3N_4), and carbon nanotubes (CNTs), were evaluated for effective photodegradation of organic pollutants and photoelectrochemical (PEC) water splitting. These hybrids are formed at room temperature using sonication, and were shown to be effective for photodegradation of Rhodamine B (RhB) under irradiation with visible light. The hybrids samples resulted in a significant increase in photocatalytic activity compared with single-component samples of g-C_3N_4. In particular, the g-C_3N_4/CNTs/Au hybrids exhibited an exponential increase in the photocatalytic activity by a factor of almost 40. Structural and compositional analyses show the successful formation of ternary g-C_3N_4/CNTs/Au hybrids. The SPR due to the Au nanoparticles led to high optical absorbance, and the inclusion of the CNTs led to effective separation of photogenerated charge carriers, resulting in substantial improvement of the photocatalytic properties. PEC measurements indicate effective use of charge carriers, and open-circuit voltage decay measurements demonstrated increased lifetime of the photogenerated charge carriers in the hybrid samples. The ternary g-C_3N_4/CNTs/Au sample resulted in a large specific surface area, providing a large number of active sites for the adsorption of organic molecules. Therefore, a facile and room temperature fabrication method was shown to introduce Au and CNTs in the hybrid for substantial improvement of photocatalytic activities and effective water splitting.

Keywords: Semiconductors, Carbon nanotubes, Hybrids, Photocatalysis, Photoelectrochemical cell

Corresponding Author: Caroline Sunyong Lee (sunyonglee@hanyang.ac.kr)

Introduction

The considerable and global growth of industrial activity in recent decades has resulted in serious impacts on the environment, polluting the air and water, generating large amounts of waste, and threatening environmental sustainability [1]. In particular, deteriorations in water quality and quantity today are a major concern facing almost all countries. A number of reports have examined the development of cost effective and viable techniques for remediation and purification of polluted water, including chemical treatments, boiling, sedimentation, and filtration [2]. However, these techniques do not fulfill water quality standards and are not sufficient for purification because of the large quantities of polluted water. Photocatalytic degradation of water in the presence of heterogeneous semiconductor photocatalysts has been shown to have significant potential as a low-cost, environmentally sustainable technology for water purification [3]. It has several advantages over conventional methods, including the ability to degrade a wide range of toxic compounds and to exploit solar energy and transfer pollutants from one medium to another; furthermore, it is applicable to gaseous and aqueous treatments, and requires a relatively short process time [4]. Numerous reports have discussed the design and development of a variety of photocatalysts for use in air or water purification applications [5]. Primarily, combinations of metal/metal oxide nanostructures (including Au, Ag, Pt, TiO_2, ZnO, SnO_2, WO_3, Nb_2O_5, $BiVO_4$, and Fe_2O_3) and conducting polymers (polyaniline, polypyrrole, and polythiophene) have been investigated for the degradation of organic pollutants and carcinogenic materials [6]. These photocatalysts have shown promising photocatalytic activity toward the degradation of a wide range of organic pollutants under irradiation with ultraviolet (UV) and visible light. Nevertheless, these photocatalysts are not environmentally benign, and they suffer from efficiency issues, limiting their practical use.

Recently, polymeric graphitic carbon nitride (g-C_3N_4) has emerged as a promising candidate for metal–oxide photocatalysts because of the narrow band gap (~2.7 eV), the absence of metals, its low toxicity and favorable chemical and thermal stability, and the fact that the conjugated carbon and nitrogen structure offers coupling with a wide range of catalysts [7]. Furthermore, g-C_3N_4 has been shown to have potential applications in fuel cells, spintronics, CO_2 reduction, and hydrogen production [8]. Additionally, g-C_3N_4 has potential applications in water purification.

However, during photocatalysis, it suffers from a high charge carrier recombination rate and from slow electron transfer due to the weak interaction between neighboring planes, and it exhibits absorption only at relatively short wavelengths (<460 nm), all of which lead to poor photocatalytic performance [9]. A number of approaches are available to address these issues, including doping, controlling the surface morphology, increasing the surface area, forming hybrids with carbonaceous materials, and the use of metal/metal oxide nanostructures and polymers [10]. Among these, sensitization with metal nanoparticles (namely Au, Ag, Pt and Pd) and carbon-based materials (CNTs and graphene) are the most viable routes for the fabrication of g-C_3N_4-based photocatalysts [11]. Metal nanoparticles have gained considerable attention because of surface plasmon resonance (SPR), which gives rise to strong absorption of visible light, and because the metal particles act as trapping sites for electrons, improving its separation of electron–hole pairs [12]. The wavelength range for optical absorption can be tuned by adjusting the dimensions of the metal nanoparticles or the nature of the surrounding material, which affects the photocatalytic activity [13]. Moreover, metal nanoparticles exhibit resonant photon scattering, which increases the interaction time with the catalyst and generates more electron–hole pairs [14]. Among these, Au nanoparticles have been most studied until now even though it is relatively expensive because of its unique physiochemical properties, such as biocompatibility and amphilicity, and surface carrier capabilities. Moreover, quick and easy synthesis using Turkevich method, shows shape and size dependent electrochemical and optical properties [15]. Hybrids loaded with Au nanoparticles have shown improved photodegradation compared with that of g-C_3N_4 [16,17]. Additionally, there have been reports of further increases in the photocatalytic performance of g-C_3N_4 using carbon-based materials such as CNTs [18]. It is known that the metallic and one-dimensional (1D) structure of CNTs provides superior electron transport. Moreover, the large specific surface area, elasticity, high tensile strength, hollow structure, and extraordinary mechanical and electronic properties have attracted considerable attention for applications including photocatalysis, field-emission displays, chemical sensors, and energy storage [19]. CNTs can reduce the charge carrier recombination rate of semiconductor photocatalysts [20,21]. Suryawanshi *et al*. increased the rate of hydrogen production by adding functionalized CNTs to g-C_3N_4 and showed that the CNTs contributed to the charge transfer mechanism [22]. Chen *et al*. achieved an increase in the lifetime of charge

carriers by a factor of almost three due to the strong interactions between g-C_3N_4 and CNTs for applications in hydrogen production [23]. Ge and Han fabricated hybrids of CNT/g-C_3N_4 using a heat-treatment method and concluded that efficient separation of the photogenerated charge carriers resulted in a four-fold increase in the photocatalytic hydrogen production under irradiation with visible light [24].

Here, we report facile ultrasonication method for the fabrication of hybrids using Au, CNTs, and g-C_3N_4 for water purification and splitting. To the best of our knowledge, this is the first demonstration of a ternary hybrids of Au, CNTs, and g-C_3N_4 for RhB degradation under irradiation with visible light. The initial quantity of Au and CNTs on the g-C_3N_4 porous structure was optimized, as was the process, in order to achieve a uniform distribution of Au nanoparticles and CNTs in the hybrids. The structural, optical, and electrochemical properties of the samples were investigated in detail. Furthermore, visible photocatalysis measurements were carried out, demonstrating degradation of RhB, and the optimum quantities of Au and CNTs were determined. The improved activity is attributed to the large specific surface area, a reduction in the recombination losses, the favorable charge transport properties, and the high visible light absorption due to the SPR. Open-circuit potential decay (OCVD) analysis showed an increase in the lifetime of charge carriers, leading to effective separation of electrons and holes. Based on the experimental results described here, we propose two possible photocatalytic mechanisms. Re-usability tests demonstrated the stability of the Au/CNT/g-C_3N_4 hybrids over 4 cycles of photocatalysis.

Experimental section

Synthesis of photocatalysts

Reagents

Multiwall carbon nanotubes (CNTs), ~20 nm in diameter and of >95% purity, were purchased from NanoLab, Inc. (USA). Gold (III) chloride hydrate ($HAuCl_4{\cdot}xH_2O$; 99.99%) was purchased from Sigma Aldrich. All other reagents, including sodium citrate and urea, were of analytical grade, purchased from Junsei chemicals and used as received.

Synthesis of colloidal Au nanoparticles

Colloidal dispersions of Au nanoparticles were prepared using the Turkevich method [25]. Briefly, gold chloride (0.005 M) was added to 300 mL of distilled water at room temperature in a round-bottom flask, followed by vigorous stirring and heating until boiling occurred. Then, a 3-mL solution of sodium citrate (0.04 M) was added in the flask while stirring. The solution changed from yellow to colorless and then to pale red (see Figure S1); when no further color change occurred, we inferred that the reaction was complete.

Synthesis of g-C_3N_4 sheets

Sheet-like porous g-C_3N_4 structures were synthesized as described in Ref. [26]. A 20-g sample of urea powder was placed in an alumina crucible and maintained at 70°C for 1 hour. The crucible was then heated at a rate of 5°C/min to 580°C and maintained at this temperature for 2 hours under an air atmosphere, and then allowed to cool naturally until it reached room temperature. A fine yellow powder was produced for use directly in further experiments.

Fabrication of g-C_3N_4/Au, g-C_3N_4/CNTs and g-C_3N_4/CNTs/Au hybrids

The gold nanoparticles were sensitized onto g-C_3N_4 sheets using ultrasonication at room temperature. Then, 50 mg of g-C_3N_4 powder was added to 20 mL of the gold colloidal dispersion (100 vol.%) and ultrasonicated for 2 hours. The g-C_3N_4/Au dispersion was then filtered and washed several times using ethanol. The resulting Au/g-C_3N_4 powder was collected and dried overnight at 60°C. The g-C_3N_4/CNTs hybrid was synthesized by combining 60:40 mass ratio of g-C_3N_4 and CNTs. The CNTs and g-C_3N_4 powder were placed in a glass vial with 20 mL of distilled water and then sonicated for 2 hours. The resulting product was filtered and dried in an oven overnight at 60 °C. To fabricate the g-C_3N_4/CNTs/Au hybrid, a similar process was followed as above. We used what will be shown to be the optimum Au vol.% (100%), and the optimum amount of g-C_3N_4/CNTs powder was added simultaneously. The mixture was sonicated for 2 hours and filtered. The final product was dried and stored in glass vials. All of the collected powders were used for future analyses and photocatalytic evaluation.

Characterization

The crystallinity and phase of the hybrids were investigated using X-ray diffraction (XRD) (Rigaku D/MAX-2500/PC, Cu Kα, λ = 1.5418 Å). The influence of the Au and MWCNTs on the surface morphology of the g-C_3N_4 was examined using field-emission scanning electron microscopy (FESEM) (Hitachi s4800, at 15 kV). High-resolution transmission electron microscopy (HRTEM) images and selected area electron diffraction (SAED) patterns of the microstructures were examined using a JEOL 2100 transmission electron microscope (TEM) at 200 kV. Optical absorbance spectra were recorded using a UV–visible (UV-vis) spectrophotometer (V-600, Jasco, Japan) with a dry-pressed $BaSO_4$ disk used as a reference. Photoluminescence (PL) spectra were recorded at room temperature with excitation using a He-Cd laser (Dong Woo Optron, South Korea, λ_{ex} = 325nm). The specific surface area (S_{BET}) was determined using nitrogen adsorption–desorption isotherms with a Quantochrome machine cooled to liquid nitrogen temperatures (AS1), and the total pore size distribution was calculated using the Barret–Joyner–Halender (BJH) method. X-ray photoelectron spectroscopy (XPS) was used to determine the chemical composition of the hybrids (Sigma Probe; Thermo-Scientific, UK). Raman spectra were recorded at room temperature using a Renishaw Raman spectrometer with laser excitation at 785 nm. The actual amount of Au in the hybrids samples was determined using inductively coupled plasma-atomic emission spectroscopy (ICP-AES, Perkin Elmer OPTIMA 7300 DV model) analysis.

Photocatalysis

RhB was chosen as a standard organic pollutant to investigate the photocatalytic performance of the synthesized hybrid samples. All measurements were carried out at room temperature in a batch-type reactor with an aqueous solution of the RhB dye. First, 50 mg of photocatalyst was added to 250 mL of the dye solution and stirred for 1 hour in the dark to reach an equilibrium adsorption of catalysts and dye molecules. The mixture was then irradiated using a visible light source placed approximately 5 cm from reactor to supply an illumination intensity of 50 mW/cm^2. Aliquots were taken at 10-minute intervals, and the optical absorbance was measured using the UV-vis spectrophotometer. The change in the concentration of RhB was monitored

using the characteristic absorption at 553 nm. For comparison, we tested RhB degradation without the photocatalyst, as well as the photocatalytic activity of Degussa powder under the same experimental conditions. The reusability of the selective photocatalyst was investigated using a similar procedure. After each cycle, the powder photocatalyst was collected using a centrifuge and washed several times with water and ethanol. The total organic carbon (TOC) was measured using a Shimadzu TOC analyzer (TOC-V_{CSH}, Japan).

Electrochemical characterization

Photoelectrochemical (PEC) and open-circuit potential decay (OCVD) measurements were carried out using a potentiostat (VersaSTAT 4, Princeton Applied Research) with a three-electrode configuration. The working electrode was 1 × 1 cm^2 and was formed of the hybrid powder, which was deposited onto a fluorine-doped tin oxide (FTO) substrate using a Liquion solution and then dried in an oven at 60°C. The deposited films were used as the working electrode. A saturated calomel electrode (SCE) (Ag/AgCl) was used as the reference electrode, and a graphite rod was used as the counter electrode. The electrochemical measurements were carried out in a 0.5-M aqueous Na_2SO_4 redox electrolyte.

Results and discussion

XRD analysis

The effect of incorporating Au and CNTs on the structure of g-C_3N_4 was investigated using XRD analysis of pure and hybrid samples. Figure S1 shows XRD patterns of the g-C_3N_4/Au, g-C_3N_4/CNTs and g-C_3N_4/CNTs/Au hybrids with 100 vol.% of gold. Patterns for the pure g-C_3N_4 are provided for comparison. For pure g-C_3N_4, the pattern shows two broad diffraction peaks at 13.12° and 27.50°, indicating the formation of amorphous structure. These two peaks are assigned to in-plane s-triazine units and a conjugated melon structure along the (100) and (002) planes [27]. With the g-C_3N_4/Au/hybrid, additional peaks appeared at 38.18°, 44.38°, 64.57°, and 77.56°, which are attributed to a cubic phase of the gold nanoparticles (PDF#98-000-0230). Moreover, there was no change in the locations of the peaks for g-C_3N_4, indicating that the addition of Au did not affect the graphitic structure of the g-C_3N_4. Then structural changes for

the formation of g-C_3N_4/CNTs hybrid was analyzed using XRD. The XRD pattern of the CNTs is provided for comparison. The CNTs exhibited diffraction peaks at 26.3° and 42.7°, corresponding the hexagonal graphite structure in the CNTs along the (002) and (100) directions [28]. After combining CNTs with the g-C_3N_4, the XRD patterns exhibited two additional peaks, which are assigned to the g-C_3N_4 phase. Moreover, the existence of peaks related to CNTs and g-C_3N_4 indicates the formation of a hybrid. In case of g-C_3N_4/CNTs/Au hybrid, the XRD pattern exhibited peaks at the same locations as those found for the former hybrids. Therefore, it follows that Au sensitization did not affect the structure of the CNTs or of the g-C_3N_4, and the existence of peaks corresponding to Au, CNTs, and g-C_3N_4 phases supports the successful fabrication of ternary hybrid samples.

FESEM and TEM analyses

The microstructure and the surface morphology of hybrid samples were investigated using FESEM, as shown in Figure 1. A sheet-like structure with uniform micron-sized pores was formed from the g-C_3N_4, as shown in Figure 1A. The interconnected network comprised of randomly shaped sheets with several nanometers in length and a few nanometers in thickness, as shown in the high-magnification image in Figure 1A. This indicates that the g-C_3N_4 sheets were separated from each other and dispersed throughout the sample. Following Au sensitization at 100 vol.%, the surface morphology was almost unchanged, and the Au nanoparticles were densely distributed on the g-C_3N_4 sheets, as shown in Figure 1B. The magnified images show that the g-C_3N_4 sheets were almost completely covered with Au particles. In g-C_3N_4/Au sample, we could see Au particles with an average diameter of 20-nm, tethered to the g-C_3N_4 sheets. Moreover, the magnified images show that the size distribution of the Au particles was uniform for g-C_3N_4/Au sample. We may expect that a higher density of Au nanoparticles will provide more sites for the adsorption of pollutant molecules. FE-SEM images of the g-C_3N_4/CNTs hybrid are shown in Figure 1C. The CNTs were a few nanometers in diameter and several nanometers in length; these structures combined uniformly with g-C_3N_4 sheets and the sample was almost completely covered with CNTs. Figure 1D shows the morphology of ternary g-C_3N_4/CNTs/Au hybrid samples. The Au and CNTs components were both loaded onto the g-C_3N_4 sheets. However, loading with Au nanoparticles remained almost the same in the hybrids, regardless of

adding 100 vol.% of Au, as shown in the magnified images (Figure 1D). Therefore, Au, CNTs, and g-C_3N_4 sheets formed a uniform hybrid material, which is expected to reduce the recombination losses and provide more effective transfer of photoelectrons.

Figure 2A–E show TEM images of pure and hybrid samples, including SAED patterns. The spherical Au nanoparticles, whose average diameter was 20 nm, were deposited uniformly over the entire sample area, as shown in Figure 2A. The corresponding SAED patterns show that the Au nanoparticles were polycrystalline (see the magnified image in Figure 2A and inset). Figure 2B shows a number of graphitic layers stacked in large sheets several microns in size. The HRTEM image of the g-C_3N_4 shows relatively thin interconnected sheets, indicating the formation of a few layers due to ultrasonication (see the high-magnification image in Figure 2B). The poorly resolved diffraction rings in the SAED patterns suggest an amorphous g-C_3N_4 structure (see the inset of the magnified image in Figure 2B).

Figure 2C TEM images of the g-C_3N_4/Au hybrid sample formed using a 100-vol.% Au dispersion. The low magnification image shows that the surface of the g-C_3N_4 was densely and homogeneously covered with Au nanoparticles, and the particle size distribution matched that of the Au nanoparticles. The HRTEM image shows formation of a heterojunction due to the strong interaction between the g-C_3N_4 and Au particles (see the magnified image in Figure 2C). Moreover, the density of Au appears to be higher than that reported in Ref [11a]. The inset of the magnified image in Figure 2C shows the corresponding SAED pattern, which reveals the nanocrystalline nature of the g-C_3N_4/Au hybrid.

The low-magnification TEM image shown in Figure 2D reveals well-dispersed CNTs on the surface of g-C_3N_4 structure. The HRTEM image shows that the tube-like structure of CNTs, with an average diameter of 10 nm, and the thin g-C_3N_4 layer were well combined and attached each other (see the magnified image in Figure 2D). The diffused SAED pattern indicates the amorphous structure of CNTs and g-C_3N_4 hybrid (see the inset of the magnified image in Figure 2D).

Figure 2E shows TEM images of the ternary g-C_3N_4/CNTs/Au hybrid sample. It is clear that the CNTs and Au particles were dispersed onto the g-C_3N_4 sheets. The magnified TEM image of g-C_3N_4/CNTs/Au hybrid shows that ternary heterojunctions were formed between the Au, CNTs, and g-C_3N_4 components (see the magnified image Figure 2E). The existence of poorly resolved rings in the SAED pattern corresponds to the polycrystalline nature of the g-C_3N_4/CNT/Au hybrid (see the inset of the magnified image in Figure 2E). From the TEM analysis, we may expect a large specific surface area and effective transport of photoelectrons through the hybrid, which is expected to result in superior photocatalytic performance compared with that of g-C_3N_4. In addition , actual amount of gold present in the g-C_3N_4/Au and g-C_3N_4/CNTs/Au hybrid sample, was measured using ICP-AES analysis (Table 1). It is found that g-C_3N_4/CNTs/Au has relatively lower Au concentration compared with that of g-C_3N_4/Au hybrid sample. The lower amount of gold in g-C_3N_4/CNTs/Au is attributed to presence of CNTs occupying few sites of g-C_3N_4 sheets, which reduce relative gold loading as compared with that of g-C_3N_4/Au hybrid sample. However, in both hybrid samples, Au loading is pretty much high for effective optical absorbance of visible light and for effective degradation of contaminants.

Optical absorbance

Metal nanoparticles exhibit SPR, which can increase the optical absorption over a wide range of wavelengths. We carried out measurements of the optical absorbance of the Au dispersion, which exhibited a strong peak at 522 nm, as shown in Figure S2. This absorption feature corresponds to Au nanoparticles with a diameter of 20 nm [29]. We introduced these Au nanoparticles into the g-C_3N_4 network to determine the effects of the Au particles on the optical absorbance of g-C_3N_4 in the visible part of the spectrum. Figure 3 shows the optical absorbance spectra of pure g-C_3N_4, g-C_3N_4/Au and g-C_3N_4/CNTs/Au samples with 100 vol.% of Au dispersion in the wavelength ranging from 300 to 850 nm. The g-C_3N_4 sample exhibited an absorption edge at ~450 nm, which corresponds to the intrinsic band gap of 2.7 eV [30]. Following sensitization with the Au nanoparticles, the optical absorbance of g-C_3N_4 increased significantly. The SPR peak was found to occur at same wavelength as with the dispersion of Au nanoparticles. The optical absorbance of the CNTs combined with g-C_3N_4 samples, as compared with that of pure g-C_3N_4, the g-C_3N_4/CNTs hybrid showed increasing optical absorbance over

the entire range of the visible spectrum, and the absorption increased with the addition of CNTs. The absorbance of the pristine CNTs is also shown for comparison. Looking at the optical absorbance of the g-C_3N_4/CNTs/Au ternary hybrid, visible absorbance significantly increased when Au and CNTs were added to the g-C_3N_4 network. The SPR peak of Au nanoparticles was found to merge with the absorption spectrum of the CNTs due to the large optical absorbance of CNTs. The combination of Au and CNTs with g-C_3N_4 increased the absorption of visible light. It follows that we may expect that the introduction of Au and CNTs will increase the photocatalytic activity under irradiation with visible light.

Photoluminescence

Room temperature PL emission spectra are widely used to characterize the radiative recombination properties of semiconductor photocatalysts. The separation, recombination, and transport properties of photocatalysts can be analyzed using PL spectroscopy. High emission intensity of the PL spectra means that the radiative recombination rate is high. Figure 4 shows the PL spectrum of the pure g-C_3N_4, g-C_3N_4/CNTs and g-C_3N_4/CNTs/Au dispersion with 100 vol% of Au, and 60:40 mass ratio for the CNT/g-C_3N_4 sample. The presence of a strong broad emission feature around 470 nm in all samples is attributed to n-π^* transitions, as this wavelength corresponds to the band gap of g-C_3N_4 [31]. Furthermore, we can see that introducing Au to the g-C_3N_4 network reduced the PL intensity substantially compared with that of pure g-C_3N_4; this is indicative of effective separation of photogenerated electrons and holes. The PL intensity was almost 2 times smaller for the Au-sensitized g-C_3N_4 hybrids than for the pure g-C_3N_4. The intensity for the PL spectra of the g-C_3N_4/CNTs hybrid, was almost 30 times lower than that of pure g-C_3N_4 or the Au/g-C_3N_4 samples. Moreover, the quenched PL spectra for the g-C_3N_4/CNTs/Au hybrid, indicate that the integration of Au and CNTs results in a reduction for overall PL intensity, and suggest effective transport of photogenerated electrons. Similar trends have been reported previously [32–34]. We may therefore expect that the g-C_3N_4/CNTs/Au sample will exhibit favorable photocatalytic degradation of pollutants under irradiation with visible light.

Surface area and pore-size distribution

The specific surface area and pore-size distribution of the pure g-C_3N_4, 100-vol.% g-C_3N_4/Au, g-C_3N_4/CNTs (with a mass ratio of 60:40), and g-C_3N_4/CNTs/Au hybrids were measured using nitrogen adsorption–desorption and analyzed using the Brunauer–Emmett–Teller (BET) method. The obtained hysteresis loops reveal type-IV isotherms within a given relative pressure for the pure and hybrid samples. As can be seen from Figure S3A–D, the BET surface area of g-C_3N_4/CNTs/Au hybrid was found to be 120.17 m^2g^{-1}, which is almost double that of the g-C_3N_4 sample (67.19 m^2g^{-1}) and significantly larger than the g-C_3N_4/Au (71.02 m^2g^{-1}) or g-C_3N_4/CNTs (110.02 m^2g^{-1}) samples. For the g-C_3N_4 sample, the specific surface area was found to be larger than that reported previously [23,35,36]. Martha *et al.* obtained effective hydrogen production (135 μmol h^{-1}) using g-C_3N_4 with a mixture of urea and melamine, and reported a maximum specific surface area of 50 m^2g^{-1} [37]. Based on these reports, it appears that a large specific surface area results in improved performance of photocatalysts.

We have achieved larger specific surface areas than have been reported previously. This is attributed to the exfoliation of the g-C_3N_4 sheets following ultrasonication. Moreover, the combination of Au nanoparticles and CNTs appears to have a synergistic effect in increasing the specific surface area of the g-C_3N_4-based hybrid. Therefore, these hybrids are expected to provide a large number of active sites for photocatalysis, which is in turn expected to lead to high catalytic efficiency. Pore-size distribution curves are shown in the insets of Figure S3A–D. The trends were similar in all samples, including g-C_3N_4: the distribution curves of g-C_3N_4 and g-C_3N_4/Au samples showed mesoscopic pores with diameters in the range 25–60 nm, whereas the g-C_3N_4/CNTs and g-C_3N_4/CNTs/Au hybrids exhibited two peaks centered on 25 nm and 45 nm. The addition of CNTs narrowed the pore-size distribution due to the strong interaction with g-C_3N_4. The resulting smaller pores may lead to more effective charge separation and hence photocatalysis.

XPS analysis

The surface chemical composition of g-C_3N_4/CNTs/Au hybrid sample was investigated by analyzing XPS spectra. The survey spectrum has peaks corresponding to C, N, O (which we may expect to be adsorbed from the air) and Au (see Figure S4A). The C 1s core level spectra

exhibited five components at binding energies of 284.60, 285.92, 287.21, 289.40, and 291.06 eV, as shown in Figure S4B. The strongest peak, at 284.60 eV, is attributed to the graphitic structure of carbon (i.e., C–C) [38]. The two peaks at 287.21 and 289.40 eV are attributed to bonding between carbon and nitrogen from in the g-C_3N_4 [39-41]. The further two peaks at binding energies of 285.92 and 291.06 eV can be assigned to –C–C and π–π* vibrations, indicating the presence of CNTs as well as g-C_3N_4 in the hybrid sample [42,43]. The N 1s XPS spectra (see Figure S4C) exhibited an asymmetrical feature representing the existence of nitrogen in different environments [44]. Gaussian fitting gave five distinguishable peaks, at 299.95, 401.48, 402.95, 405.06 and 406.94 eV, the strongest of which, that at 399.95 eV, is attributed to the existence of tertiary nitrogen, i.e., N–$(C)_3$, which indicates a large amount of polymerization of urea [26]. The two weaker peaks, located at 401.48 and 402.95 eV, are attributed to amino functional groups N=H/-NH_2 and *n*-π transitions [45]. Moreover, the N 1s core level spectra show two additional peaks at binding energies of 405.06 and 406.94 eV can be assigned to nitrogen in the azo structure (–N=N–) and NO_2 groups [46,47]. The Au 4f core level XPS spectra were deconvoluted into two major characteristic peaks at binding energies of 84.17 and 87.79 eV, which correspond to Au $4f_{5/2}$ and Au $4f_{7/2}$ bands, respectively (see Figure S4D). Two more peaks in the Au spectrum at 85.35 and 89.01 eV peaks are attributed to the presence of Au in the form of the Au^{3+} valence state, which corresponds to the oxide state of Au. However, the Au core spectrum exhibits two strong peaks at 84.17 and 87.79 eV, confirming a large fraction of Au in the metallic state [48,49]. This confirms the presence of Au in the form of an Au^0 valence (i.e., metallic) state [50]. Additionally, a small peak was observed at 90.22 eV, which is attributed to the oxidized Au^+ state [51].

Raman spectra

Figure 5 shows Raman spectra of the g-C_3N_4, CNTs, g-C_3N_4/Au, g-C_3N_4/CNTs, and g-C_3N_4/CNTs/Au samples in the range 600–2000 cm^{-1}. The Raman spectrum of the single-component g-C_3N_4 sample exhibited three major peaks at 708, 1233, and 1561 cm^{-1}. The peak centered on 708 cm^{-1} has been reported to be related to the breathing modes of the s-triazine ring, which exists in the g-C_3N_4 network [52]. The two additional peaks at 1233 and 1561 cm^{-1} are attributed to the presence of defects or disorder in the graphite structure and the stretching modes

of the C=N bond, respectively [53]. For the g-C_3N_4/Au sample, the strong peak at 1563 cm^{-1} is associated with the C=C bond and was stronger than that with single-component g-C_3N_4; furthermore, the two peaks at 1233 and 708 cm^{-1} disappeared in the g-C_3N_4/Au sample. We suspect that Au may result in scattering modes of the g-C_3N_4 network due to scattering from the C=N bond (1561 cm^{-1}). The two major bands in the Raman spectrum of the pure CNTs spectrum, at 1305 and 1592 cm^{-1},can be assigned to amorphous carbon and graphite carbon vibrations of the C=C bond [54,55]. The Raman spectrum of g-C_3N_4/CNTs sample exhibited three major bands, out of these two at 1310 and 1597 cm^{-1} could be assigned to scattering from CNTs, additional band at 710 cm^{-1} aroused from g-C_3N_4 structure. From the peak position it is seen that there is shift in compared to pure CNTs and g-C_3N_4 spectra, which may be attributed to strong interaction between CNTs and g-C_3N_4 in the hybrid. The absence of the peaks at 1233, and 1561 cm^{-1}, which correspond to g-C_3N_4, is attributed to the low scattering intensity compared with the CNTs. For the ternary hybrid g-C_3N_4/CNTs/Au, the two major bands, located at 1308 and 1590 cm^{-1}, are attributed to combined effect of CNTs and g-C_3N_4 structures, respectively. Furthermore, these bands were stronger and broader compared with the similar features in the spectrum of the g-C_3N_4/CNTs hybrid, which is indicative of the plasmonic effects of the Au nanoparticles.

Photocatalysis

To evaluate the photocatalytic activity of the synthesized pure and hybrid samples, we investigated the photocatalytic degradation of RhB under irradiation with visible light. Figure S5 shows UV-vis optical absorbance spectra of the RhB solution irradiated under visible light in the presence of the single-component g-C_3N_4, g-C_3N_4/CNTs and g-C_3N_4/CNTs/Au samples. For comparison, the optical absorbance of the dye solutions was also measured under irradiation with visible light, but without a catalyst. It was observed that RhB peak at 553 nm decreased with increasing irradiation time in the presence of photocatalysts, whereas this peak remained unchanged without the photocatalysts. The rate of change in degradation can be quantified from the time dependence of the absorbance at 553 nm. The RhB peak decreased more rapidly for the 100-vol.% Au/g-C_3N_4 hybrid sample than with the single-component g-C_3N_4 or other hybrid samples. It has been reported that the disappearance of this peak is due to the degradation of the conjugated xanthene ring in the RhB molecule and to blue shifts due to N-deethylation [56,57].

The rapid destruction of RhB may result from enhanced optical absorbance and transportation of photoelectrons due to its presence of Au and CNTs. Additionally, Au nanoparticles have strong interaction with g-C_3N_4 network which promoted the charge separation and transportation. Because of higher absorbance caused by Au nanoparticles, these Au nanoparticles assist large number of generation of electron-hole pairs and increased rate of oxidation-reduction reactions. The incorporation of CNTs has synergistic effect in terms of dye molecule adsorption on the surface of hybrid samples because of large surface area. Its tremendous electron mobility helps rapid separation of electron-hole pairs and transportation, resulting in loss of RhB molecules. These results were further analyzed by calculating the change in the absorbance as a function of time during irradiation. For comparison, results are also shown for powder samples of a commercially available photocatalyst P25 (Degussa). Figure 6A shows that the concentration of RhB declined substantially faster for the g-C_3N_4/CNTs/Au (100 vol.%) than for the single-component g-C_3N_4 and the other hybrid samples. With no photocatalyst, there was no change in the RhB concentration, revealing that degradation did not occur under irradiation with visible light without a catalyst. The introduction of Au and CNTs to g-C_3N_4 resulted in significant improvement in the photocatalytic performance of g-C_3N_4. The P25 sample exhibited poor photocatalytic activity under irradiation with visible light because of the wide band gap (3.2 eV).

The reaction kinetics was investigated by fitting the decay of the peak at 533 nm to $\ln(A_0/A) = kt$, where k is the apparent kinetic rate constant, A_0 is the initial absorbance of RhB solution, and A is the RhB absorbance at time t. The logarithmic plots shown in Figure 6B describe straight lines, corresponding to pseudo-first-order kinetics. The calculated rates constants are listed in Table 1. The largest kinetic rate constant was for the 60:40 hybrid with Au (41.10 min^{-1}), which is substantially larger than that for the single-component g-C_3N_4 photocatalyst (0.46 min^{-1}) and other hybrids i.e. g-C_3N_4/Au (3.28 min^{-1}) and g-C_3N_4/CNTs (27.29 min^{-1}). Based on these data, it appears that the combination of Au and CNTs with the g-C_3N_4 hybrid lowered the recombination losses remarkably, providing favorable photocatalytic performance. We monitored the photodegradation process by measuring the TOC of the degraded solution following the optical absorbance measurements (see Table 1). The TOC for g-C_3N_4/CNTs/Au sample was found to be the lowest, which indicates that this was the most effective photocatalyst

for RhB under irradiation with visible light. The favorable performance of the Au/CNT/g-C_3N_4 hybrid is attributed to the following effects: (i) SPR due to the Au nanoparticles, which leads to large optical absorbance; (ii) effective transfer of photoelectrons via the CNTs; and (iii) the large specific surface area, which provides many sites for adsorption of RhB molecules.

Possible photodegradation mechanisms

For the single-component g-C_3N_4, the degradation was slow because of the small optical absorbance at visible wavelengths, as well as due to the large recombination losses. To improve the photocatalytic performance, it is necessary to combine it with another semiconductor (or conducting material) to achieve rapid transport of charge carriers as well as high optical absorbance. We incorporated Au and CNTs into g-C_3N_4 to form hybrid materials with increased absorbance at visible wavelengths and improved charge transport properties. The PEC and OCVD analyses indicate minimum recombination losses, as well as long lifetimes for the photoelectrons. Moreover, the ternary hybrid sample exhibited a large specific surface area, which may be expected to facilitate many sites for the adsorption of organic compounds.

Schematic 1 shows a possible photocatalysis mechanism for the ternary g-C_3N_4/CNTs/Au hybrid material. It has been reported that Au and CNTs have strong electron affinity to capture electrons from the conduction band of g-C_3N_4 [11a, 21]. Additionally, Au exhibits strong absorbance at visible wavelengths due to the SPR, which aids in the photogeneration of electron–hole pairs. Here, we describe two possible pathways for photocatalysis. With the first (A), the band structure of the Au and CNTs provides a favorable energetic environment for rapid electron transport. Under irradiation with visible light, electrons are excited from the valence band (VB) of g-C_3N_4 to the conduction band (CB), resulting in electron–hole pairs. The CB of g-C_3N_4 (−3.38 eV *vs*. vacuum) is less negative than is the work function of the CNTs (−4.8 eV *vs*. vacuum); therefore, photoelectrons from the CB of g-C_3N_4 are captured by the CNTs [58–60]. These electrons are subsequently transferred to Au (−5.1 eV *vs*. vacuum), leading to separation of the charge carriers and hence long carrier lifetimes, reducing the recombination losses and thereby allowing for a large amount of electron–hole pairs to be available for photodegradation. The most important reaction steps in this process are described by equations I–V [61-65]:

(A) $$Au + CNTs + g - C_3N_4 \xrightarrow{hv} g - C_3N_4(h^+_{VB}) + CNTs(e^-) + Au(e^-) \quad (I)$$

$$Au(e^-) + O_2 \rightarrow Au + O_2^- \quad (II)$$

$$.O_2^- + HO_2^{\cdot} + H^+ \rightarrow H_2O_2 + O_2 \quad (III)$$

$$H_2O_2 + .O_2^- \rightarrow .OH + OH^- + O_2 \quad (IV)$$

$$H_2O_2 + e^-_{CB} \rightarrow .OH + OH^- \quad (V)$$

In the first step, due to the band-gap energy of g-C_3N_4, which corresponds to visible wavelengths, photons are absorbed, generating electron–hole pairs (Eq. I). The electrons are captured by the CNTs and transferred to the Au nanoparticles (Eq. II). The captured electrons react with dissolved oxygen molecules and produce transient superoxide radicals (Eq. III). The RhB molecules are then oxidized by reactive OH· radicals, as shown in Eqs. IV and V.

The second scheme (B) is as follows. A Schottky junction is formed between the Au and g-C_3N_4 [66–70]. Under irradiation with visible light, the SPR resulting from the Au nanoparticles generates hot electrons, which are injected into the CB of the g-C3N4 network (Eq. VI). These electrons are then captured by the CNTs, resulting in effective charge separation and photocatalytic activity (VII). A similar process then follows to generate superoxide radicals, and the degradation of RhB proceeds as described in Eqs. III–V.

(B) $$Au + CNTs + g - C_3N_4 \xrightarrow{hv} g - C_3N_4(e^-_{CB}) + CNTs(e^-) + Au(h^+_{SPR}) \quad (VI)$$

$$CNTs(e^-) + O_2 \rightarrow CNTs + O_2^- \quad (VII)$$

PEC measurements

The current–voltage (*I-V*) characteristics of the single-component g-C_3N_4, as well as the g-C_3N_4/Au, g-C_3N_4/CNTs, and g-C_3N_4/CNTs/Au hybrid samples, were measured to study the charge transport properties of the materials under irradiation with visible light, as shown in Figure 7. It is clear that the g-C_3N_4/CNTs/Au hybrid exhibited the largest photocurrent. Furthermore, all samples exhibited good stability over five on–off cycles, with very little change in the photocurrent.

Open-circuit voltage decay

OCVD measurements were used to investigate the electron transfer kinetics and recombination losses. Under irradiation with visible light, photoelectrons accumulate on the surface of the semiconductor. Following termination of the irradiation, these electrons react with the electrolyte. OVCD provides a direct measurement of the recombination rate of conduction band electrons [71,72]. We measured the OCVD by switching off the irradiation. Figure 8 shows the OCVD curves for the single-component g-C_3N_4 and the g-C_3N_4/Au, g-C_3N_4/CNTs, and g-C_3N_4/CNTs/Au hybrid samples. The potential decreased rapidly following the termination of irradiation for the single-component g-C_3N_4 and g-C_3N_4/Au samples; however, the potential decay was significantly slower for the g-C_3N_4/CNTs/Au hybrid. It follows that the ternary hybrid exhibits a slower charge carrier recombination rate.

Re-usability test

Reuse of photocatalysts is an important factor for practical applications. Figure 9 shows four consecutive cycles of photo catalysis of RhB under irradiation with visible light. There was no significant change in the photocatalytic activity over the four cycles, which indicates good stability and recyclability of the g-C_3N_4/CNTs/Au hybrid. Hence, this ternary hybrid has potential applications in the degradation of organic pollutants and the remediation of water quality.

Conclusions

We have described the fabrication and characterization of plasmonic-enhanced hybrid photocatalysts based on g-C_3N_4, CNTs and Au nanoparticles. The fabrication process proceeded at room temperature using ultrasonication. The photocatalysts were used to degrade RhB under irradiation with visible light. It was found that a 100-vol.% Au dispersion with a 60:40 mass ratio of g-C_3N_4 to CNTs exhibited optimal photocatalytic activity, exceeding that of the single-component g-C_3N_4 by a factor of approximately 40. This improvement in performance is attributed to the effective separation of charge carriers, the plasmon-enhanced absorption of visible light, and the large specific surface area for adsorption of RhB. PEC and OCVD measurements showed that the ternary hybrid resulted in rapid charge transport and long lifetimes of photogenerated electrons. Furthermore, the ternary catalyst was highly stable and could be re-used after four consecutive cycles without any noticeable change in the photocatalytic performance. Various analyses showed that Au, CNTs, and g-C_3N_4 were present in the ternary hybrids and formed pure phases. This work demonstrates that the incorporation of Au and CNTs with g-C_3N_4 results in photocatalysts with potential applications in water purification and large-scale environmental remediation, and this can be achieved using low-cost methods.

Acknowledgments

This work was supported by the National Research Foundation of Korea (NRF) grant funded by the Korea government (MEST) (2012R1A2A2A01047189), by the National Research Foundation of Korea (NRF) grant funded by the Korea government (MEST) (No.2012-0008727), and by an NRF grant funded by the Korean government (MEST) (2013R1A1A2074605).

References

[1] a) M. A. Shannon, P. W. Bohn, M. Elimelech, J. G. Georgiadis, B. J. Marinas, A. M. Mayes, Nature **2008,** 452, 301; b) M. N. Chong, B. Jin, C. W. Chow, C. Saint, Water Res. 2010, **44,** 2997; c) M. R. Hoffmann, S. T. Martin, W. Choi, D. W. Bahnemann, Chem. Rev. 1995, **95,** 69.

[2] a) R. Andreozzi, V. Caprio, A. Insola, R. Marotta, Catal. Today 1999, **53,** 51; b) A. Fujishima, T. N. Rao, D. A. Tryk, J. Photochem. Photobiol. C: Photochem. Rev. 2000, **1,** 1; c) R. Molinari, M. Mungari, E. Drioli, A. D. Paola, V. Loddo, L. Palmisano, M. Schiavello, Catal. Today 2000, **55,** 71; d) U. I. Gaya, A. H. Abdullah, J. Photochem. Photobiol. C: Photochem. Rev. 2008, **9,** 1.

[3] a) A. Fujishima, K. Honda, Nature 1972, **238,** 37; b) K. Takanabe, K. Domen, ChemCatChem 2012, **4,** 1485; c) A. Mills, R. H. Davies, D. Worsley, Chem. Soc. Rev. 1993, **22,** 417.

[4] a) G. Palmisano, V. Augugliaro, M. Pagliaro, L. Palmisano, Chem. Comm. 2007, **33,** 3425; b) R. M. Yerga, M. C. Galvan, F. Valle, J. A. Mano, J. G. Fierro, ChemSusChem 2009, **2,** 471; c) H. Tong, S. Ouyang, Y. Bi, N. Umezawa, M. Oshikiri, J. Ye, Adv. Mater. 2012, **24,** 229; d) N. Herron, W. E. Farneth, Adv. Mater. 1996, **8,** 959; e) W. Tu, Y. Zhou, Z. Zou, Adv. Mater. 2014, **26,** 4607.

[5] a) S. Das, W. M. A. Wan Daud, Renew. Sustain. Energy Rev. 2014, **39,** 765; b) M. A. Fox, M. T. Dulay, Chem. Rev. 1993, **93,** 341; c) J. C. Colmenares, R. Luque, Chem. Soc. Rev. 2014, **43,** 765.

[6] a) S. C. Warren, E. Thimsen, Energy Environ. Sci. 2012, **5,** 5133; b) C. Li, P. Zhang, R. Lv, J. Lu, T. Wang, S. Wang, H. Wang, J. Gong, Small 2013, **9,** 3951; c) H. Xu, S. Ouyang, L. Liu, P. Reunchan, N. Umezawa, J. Ye, J. Mater. Chem. A 2014, **2,** 12642; d) T. Reimer, I. Paulowicz, R Roder, S. Kaps, O. Lupan, S. Chemnitz, W. Benecke, C. Ronning, R. Adelung, Y. K. Mishra, ACS Appl. Mater. Interfaces 2014, **6,** 7806; e) D. Wang, D. Astruc, Chem. Rev. 2014, **114,** 6949; f) L. Ge, C. Han, J. Liu, J. Mater. Chem. 2012, **22,** 11843, g) L. Ge, C. Han, X. Xiao, L. Guo, Int. J. Hydrogen Energy 2013, **38,** 6960, h) F. Jiang, T. Yan, H. Chen, A. Sun, C. Xu, X.

Wang, Appl. Surf. Sci. 2014, **295,** 164, i) H. Wang, J. Lu, F. Wang, W. Wei, Y. Chang, S. Dong, Ceram. Int. 2014, **40,** 9077.

[7] a) Y. Wang, X. Wang, M. Antonietti, Angew. Chem. Int. Ed. **2012,** 51, 68; b) X. Wang, S. Blechert, M. Antonietti, ACS Catal. 2012, **2,** 1596; c) X. Wang, K. Maeda, A. Thomas, K. Takanabe, G. Xin, J. M. Carlsson, K. Domen, M. Antonietti, Nat. Mater. 2009, **8,** 76; d) X. Li, S. Zhang, Q. Wang, Phys. Chem. Chem. Phys. 2013, **15,** 7142, e) C. Han, L. Ge, C. Chen, Y. Li, X. Xiao, Y. Zhang, L. Guo, Appl. Catal. B Environ 2014, **147,** 546.

[8] a) Y. Zheng, J. Liu, J. Liang, M. Jaroniec, S. Z. Qiao, Energy Environ. Sci. 2012, **5,** 6717; b) D. Gao, Q. Xu, J. Zhang, Z. Yang, M. Si, Z. Yan, D. Xue, Nanoscale 2014, **6,** 2577; c) A. Du, S. Sanvito, S. C. Smith, Phys. Rev. Lett. 2012, **108,** 197207; c) F. Goettmann, A. Thomas, M. Antonietti, Angew. Chem. Int. Ed. 2007, **46,** 2717, d) S. Cao, J. Yu, J. Phys. Chem. Lett. 2014, **5,** 2101.

[9] a) X. Chen, J. Zhang, X. Fu, M. Antonietti, X. Wang, J. Am. Chem. Soc. 2009, **131,** 11658; b) Y. Zhang, M. Antonietti, Chem. Asian J. 2010, **5,** 1307; c) Y. Zhang, T. Mori, J. Ye, M. Antonietti, J. Am. Chem. Soc. 2010, **132,** 6294.

[10] a) M. Tahir, C. Cao, F. K. Butt, S. Butt, F. Idrees, Z. Ali, I. Aslam, M. Tanveer, A. Mahmood, N. Mahmood, CrstEngComm 2014, **16,** 1825; b) K. Dai, L. Lu, Q. Liu, G. Zhu, X. Wei, J. Bai, L. Xuan, H. Wang, Dalton Trans. 2014, **43,** 6295; c) B. Chai, T. Peng, J. Mao, K. Lia, L. Zan, Phys. Chem. Chem. Phys. 2012, **14,** 16745; d) S. Zhang, L. Zhao, M. Zeng, J. Li, J. Xu, X. Wang, Catal. Today 2014, **224,** 114.

[11] a) N. Cheng, J. Tian, Q. Liu, C. Ge, A. H. Qusti, A. M. Asiri, A. Youbi, X. Sun, ACS Appl. Mater. Interfaces 2013, **5,** 6815; b) Y. Yang, Y. Guo, F. Liu, X. Yuan, Y. Guo, S. Zhang, W. Guo, M. Huo, Appl. Catal. B Environ 2013, **142-143,** 828, c) K. Sridharan, T. Kuriakose, R. Philip, T. J. Park, Appl. Surf. Sci. 2014, **308,** 139.

[12] P. Wang, B. Huang, Y. Dai, M. H. Whangbo, Phys. Chem. Chem. Phys. 2012, **14,** 9813.

[13] a) K. Awazu, M. Fujimaki, C. Rockstuhl, J. Tominaga, H. Murakami, Y. Ohki, N. Yoshida, T. Watanabe, J. Am. Chem. Soc. 2008, **130,** 1676; b) S. Linic, P. Christopher, D. B. Ingram, nat. Mater. 2011, **10,** 911.

[14] Z. Zheng, B. Huang, X. Qin, X. Zhang, Y. Dai, M. H. Whangbo, J. Mater. Chem. 2011, **21,** 9078.

[15] a) X. Huang, M. A. EI-Sayed, J. Adv. Res. 2010, **1,** 13; b) S. Eustis, M. A. EI-Sayed, Chem. Soc. Rev. 2006, **35,** 209; c) C. T. Campbell, J. C. Sharp, Y. X. Yao, E. M. Karp, T. L. Silbaugh, Faraday Discuss. 2011, **152,** 227.

[16] L. Ge, C. Han, J. Liu, Y. Li, Appl. Catal. B Environ 2011, **409-410,** 215.

[17] L. Xu, H. Li, J. Xia, L. Wang, H. Xu, H. Ji, H. Li, K. Sun, Mater. Lett. 2014, **128,** 349.

[18] Y. Xu, H. Xu, L. Wang, J. Yan, H. Li, Y. Song, L. Huang, G. Cai, Dalton Trans. 2013, **42,** 7604.

[19] M. Volder, S. H. Tawfick, R. H. Baughman, A. J. Hart, Science 2013, **339,** 535.

[20] Y. K. Kim, H. Park, Energy Environ. Sci. 2011, **4,** 685.

[21] R. C. Pawar, D. H. Choi, C. S. Lee, Int. J. Hydrogen Energy 2015**, 40,** 767.

[22] A. Suryawanshi, P. Dhanasekaran, D. Mhamane, S. Kelkar, S. Patil, N. Gupta, S. Ogale, Int. J. Hydrogen Energy 2012, **37,** 9584.

[23] Y. Chen, J. Li, Z. Hong, B. Shen, B. Lin, B. Gao, Phys. Chem. Chem. Phys. 2014, **16,** 8106.

[24] L. Ge, C. Han, J. Liu, Y. Li, Appl. Catal. B Environ 2012, **117-118,** 268.

[25] J. Kimling, M. Maier, B. Okenve, V. Kotaidis, H. Ballot, A. Plech, J. Phys. Chem. B 2006, **110,** 15700.

[26] J. Liu, T. Zhang, Z. Wang, G. Dawson, W. Chen, J. Mater. Chem. 2011, **21,** 14398.

[27] H. Zhang, A. Yu, J. Phys. Chem. C. 2014, **118,** 11628.

[28] A. F. Shojaei, K. Tabatabaeian, F. Shirini, S. Z. Hejazi, RSC Adv. 2014, **4,** 9509.

[29] C. Ziegler, A. Eychmuller, J. Phys. Chem. C 2011, **115,** 4502.

[30] S. Chu, Y. Wang, Y. Guo, J. Feng, C. Wang, W. Luo, X. Fan, Z. Zou, ACS Catal. 2013, **3,** 912.

[31] A. Thomas, A. Fischer, F. Goettmann, M. Antonietti, J. O. Muller, R. Schlogl, J. M. Carlsson, J. Mater. Chem. 2008, **18,** 4893.

[32] Y. Sui, J. Liu, Y. Zhang, X. Tian, W. Chen, Nanoscale 2013, **5,** 9150.

[33] S. Zhang, J. Li, M. Zeng, G. Zhao, J. Xu, W. Hu, X. Wang, ACS Appl. Mater. Interfaces 2013, **5,** 12735.

[34] G. Liao, S. Chen, X. Quan, H. Yu, H. Zhao, J. Mater. Chem. 2012, **22,** 2721.

[35] J. Mao, K. Li, T. Peng, Catal. Sci. Technol. 2013, **3,** 2481.

[36] M. Zhang, J. Xu, R. Zong, Y. Zhu, Appl. Catal. B Environ 2014, **147,** 229.

[37] S. Martha, A. Nashim, K. M. Parida, J. Mater. Chem. A 2013, **1,** 7816.

[38] G. Dong, L. Zhang, J. Mater. Chem. 2012, **22,** 1160.

[39] R. C. Dante, P. M. Ramos, A. C. Guimaraes, J. M. Gil, Mater. Chem. Phys. 2011, **130,** 1094.

[40] Q. Lv, C. Cao, C. Li, J. Zhang, H. Zhu, X. Kong, X. Duan, J. Mater. Chem. 2003, **13,** 1241.

[41] S. Zhang, J. Li, M. Zeng, G. Zhao, J. Xu, W. Hu, X. Wang, ACS Appl. Mater. Interfaces 2013, **5,** 12735.

[42] D. Gao, Q. Xu, J. Zhang, Z. Yang, M. Si, Z. Yan, D. Xue, Nanoscale 2014, **6,** 2577.

[43] H. Dai, X. Gao, E. Liu, Y. Yang, W. Q. Hou, L. M. Kang, J. Fan, X. Hu, Diamond Relat. Mater. 2013, **38,** 109.

[44] M. P. Casaletto, A. Longo, A. Martorana, A. Prestianni, A. M. Venezia, Surf. Interface Anal. 2006, **38,** 215.

[45] H. F. Li, N. Zhang, P. Chen, M. F. Luo, J. Q. Lu, Appl. Catal. B Environ 2011, **110,** 279.

[46] a) S. Choi, H. Im, J. Kim, Nanotechnology, 2012, **23,** 065303; b) T. I. T. Okpalugo, P. Papakonstantinou, H. Murphy, J. McLaughlin, N. M. D. Brown, Carbon 2005, **43,** 153.

[47] C. H. Wong, M. Pumera, J. Mater. Chem. A 2014, **2,** 856.

[48] T. Odedairo, J. Ma, Y. Gu, J. Chen, X. S. Zhao, Z. Zhu, J. Mater. Chem. A 2014, **2,** 1418.

[49] X. Zhang, Dissertation Helmholtz Zentrum Beralin, 2011, Chapter 4, p. 93 (ISSN 1868-5781).

[50] J. P. Sylvestre, S. Poulin, A. V. Kabashin, E. Sacher, M. Meunier, J. H. Luong, J. Phys. Chem. B 2004, **108,** 16864.

[51] A. M. Visco, F. Neri, G. Neri, A. Donato, C. Milone, S. Galvagno, Phys. Chem. Chem. Phys. 1999, **1,** 2869.

[52] S. Tonda, S. Kumar, S. Kandula, V. Shanker, J. Mater. Chem. A 2014, **2,** 6772.

[53] P. V. Zinin, L. C. Ming, S. K. Sharma, V. N. Khabashesku, X. Liu, S. Hong, S. Endo, T. Acosta, Chem. Phys. Lett. 2009, **472,** 69.

[54] C. Wu, Z. Wang, L. Wang, P. T. Williams, J. Huang, RSC Adv. 2012, **2,** 4045

[55] A. C. Ferrari, J. Robertson, Phys. Rev. B 2000, **61,** 14095.

[56] T. S. Natrajan, M. Thomas, K. Natarajan, H. C. Bajaj, R. J. Tayade, Chem. Eng. J. 2011, **169,** 126.

[57] X. Li, J. Ye, J. Phys. Chem. C 2007, **111,** 13109.

[58] N. D. Lang, W. Kohn, Phys. Rev. B 1971, **3,** 1215.

[59] L. Sun, Y. Qi, C. J. Jia, Z. Jin, W. Fan, Nanoscale 2014, **6,** 2649.

[60] W. Wang, C. Lu, Y. Ni, Z. Xu, Appl. Catal. B Environ. 2013, **129,** 606.

[61] J. Yang, D. Wang, H. Han, C. Li, Acc. Chem. Res. 2013, **46,** 1900.

[62] Y. Li, H. Zhang, P. Liu, D. Wang, Y. Li, H. Zhao, Small 2013, **9,** 3336.

[63] L. Ye, J. Liu, Z. Jiang, T. Peng, L. Zan, Appl. Catal. B Environ 2014, **142-143,** 1.

[64] S. C. Yan, Z. S. Li, Z. G. Zou, Langmuir 2009, **25,** 10397.

[65] R. C. Pawar, V. Khare, C. S. Lee, Dalton Trans. 2014, **43,** 12514.

[66] R. C. Pawar, C. S. Lee, Appl. Catal. B Environ. 2014, **144,** 57.

[67] Y. Bu, Z. Chen, W. Li, Appl. Catal. B Environ 2014, **144,** 622.

[68] Y. Liu, Y. X. Yu, W. D. Zhang, Int. J. Hydrogen Energy 2014, **39,** 9105.

[69] C. He, Z. Zheng, H. Tang, L. Zhao, F. Lu, J. Phys. Chem C 2009, **113,** 10323.

[70] S. Yang, Y. G. Gong, J. Zhang, L. Zhan, L. Ma, Z. F. Robert, V. X. Wang, P. M. Ajayan, Adv. Mater. 2013, **25,** 2452.

[71] P. C. Liner, J. Electrochem. Soc. 1960, **107,** 343.

[72] K. S. Rao, Y. N. Mohapatra Appl. Phys. Lett. 2014, **104,** 203303.

Figure Captions

Fig. 1. FE-SEM images of (a) the single-component g-C_3N_4, (b) the g-C_3N_4/Au, (c) the g-C_3N_4/CNTs hybrid formed with mass ratio of 60:40, and (d) the ternary g-C_3N_4/CNTs/Au hybrid formed with 100-vol.% Au dispersions with g-C_3N_4 /CNTs mass ratio of 60:40. All images were acquired at magnifications of ×50,000 and ×150,000.

Fig. 2. Low- and high-magnification TEM images of (a) Au nanoparticles, (b) g-C_3N_4, (c) the Au/g-C_3N_4 hybrid formed with the 100-vol.% Au dispersion, (d) the CNT/g-C_3N_4 hybrid with a 40:60 mass ratio, and (e) the ternary Au/CNT/g-C_3N_4 hybrid formed with a CNT/g-C_3N_4 mass ratio of 40:60 and the 100-vol.% Au dispersion. The insets show the corresponding SAED patterns.

Fig. 3. Optical absorbance spectra of the single-component g-C_3N_4, g-C_3N_4/Au hybrid sample with 100 vol.% Au dispersion, g-C_3N_4/CNTs hybrid with mass ratio of 60:40 and ternary g-C_3N_4/CNTs/Au hybrid with the 100-vol.% Au dispersion.

Fig. 4. The room-temperature PL spectra recorded in the wavelength range 350–700 nm at an excitation wavelength of 325 nm, single-component g-C_3N_4, g-C_3N_4/Au hybrid sample with 100 vol.% Au dispersion, g-C_3N_4/CNTs hybrid with mass ratio of 60:40 and ternary g-C_3N_4/CNTs/Au hybrid with the 100-vol.% Au dispersion. Inset shows magnified PL emission spectra of g-C_3N_4/CNTs and g-C_3N_4/CNTs/Au hybrids.

Fig. 5. Raman spectra for the single-component g-C_3N_4, g-C_3N_4/Au hybrid sample with 100 vol.% Au dispersion, g-C_3N_4/CNTs hybrid with mass ratio of 60:40 and ternary g-C_3N_4/CNTs/Au hybrid with the 100-vol.% Au dispersion.

Fig. 6. (a) Relative optical absorbance and (b) a plot of $\ln(A_0/A)$ as a function of time for P25, g-C_3N_4, g-C_3N_4/Au, g-C_3N_4/CNTs and g-C_3N_4/CNTs/Au hybrid samples formed with 100 vol.% Au dispersions. The absorbance of RhB under irradiation with visible light without a catalyst is also shown for comparison.

Fig. 7. Photoelectrochemical measurements showing the transient response of g-C_3N_4, g-C_3N_4/Au, g-C_3N_4/CNTs and g-C_3N_4/CNTs/Au hybrid samples The measurements were taken under irradiation with visible light and in a 0.5 M Na_2SO_4 electrolyte.

Fig. 8. OCVD analyses showing the transient response of g-C_3N_4, the g-C_3N_4/Au hybrid with 100-vol.% Au dispersion, the g-C_3N_4/CNTs hybrid with a mass ratio of 60:40, and the ternary g-C_3N_4/Au/CNT hybrid with a g-C_3N_4/CNTs mass ratio of 60:40 and formed using the 100-vol.% Au dispersion. The measurements were carried out under irradiation with visible light and in a 0.5 M Na_2SO_4 electrolyte.

Fig.9. Re-usability test for the ternary g-C_3N_4/CNTs/Au hybrid with a g-C_3N_4/CNTs mass ratio of 60:40 formed using the 100-vol.% Au dispersion over four cycles.

Table 1 The calculated reaction rate constants (min^{-1}) and total organic carbon (μgCL^{-1}) for P25, g-C_3N_4, g-C_3N_4/Au hybrids with various vol.% Au dispersions, g-C_3N_4/CNTs hybrids with various CNT/g-C_3N_4 mass ratios, and the ternary g-C_3N_4/CNTs/Au hybrids formed using the 100-vol.% Au dispersion. Further, amount of Au in g-C_3N_4/Au and g-C_3N_4/CNTs/Au hybrids measured from ICP-AES technique, is provided.

Schematic 1: The photogeneration and electron transport mechanism under irradiation with visible light for degradation of organic compounds with the ternary g-C_3N_4/CNTs/Au hybrid.

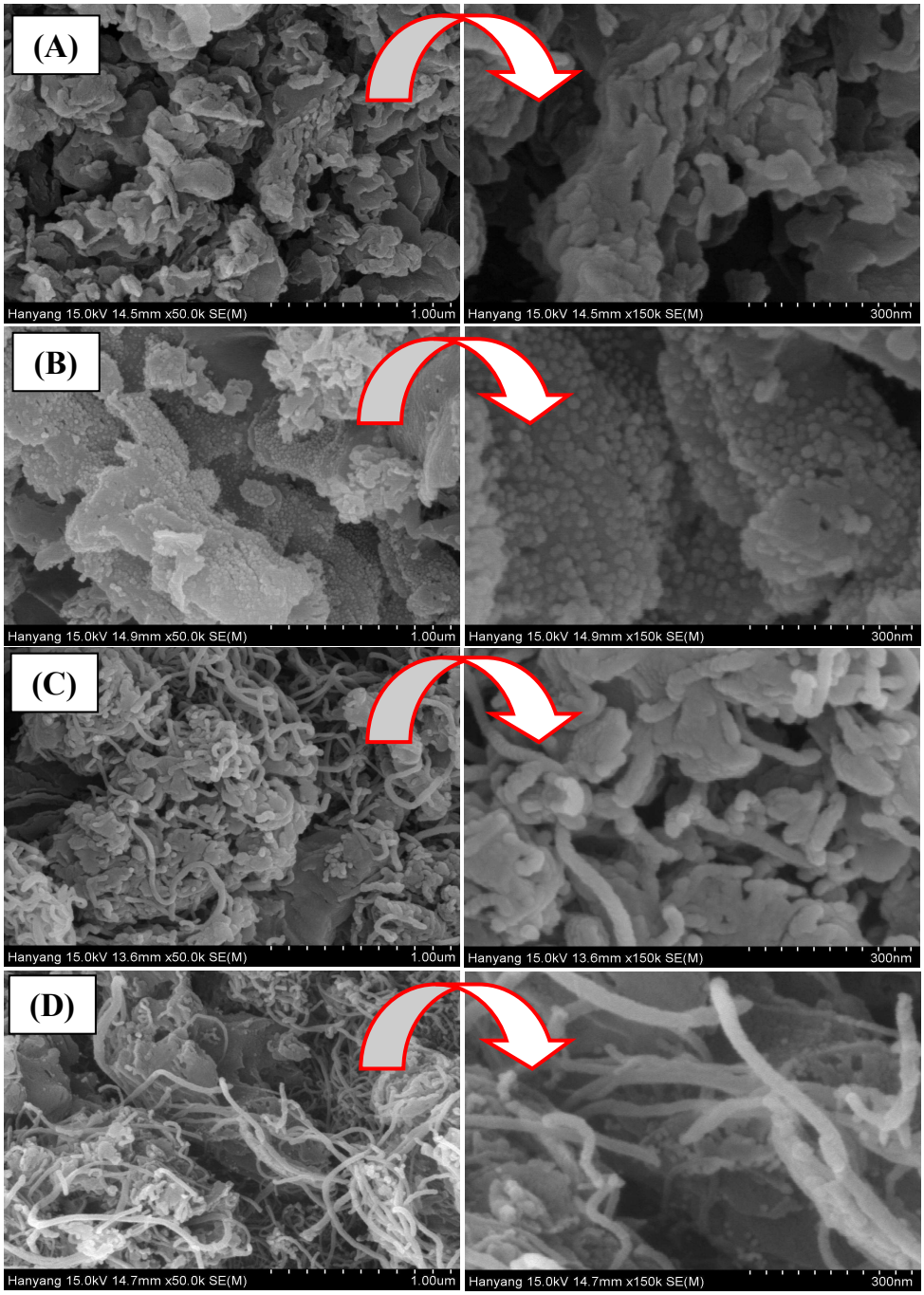

Figure 1(A to D)

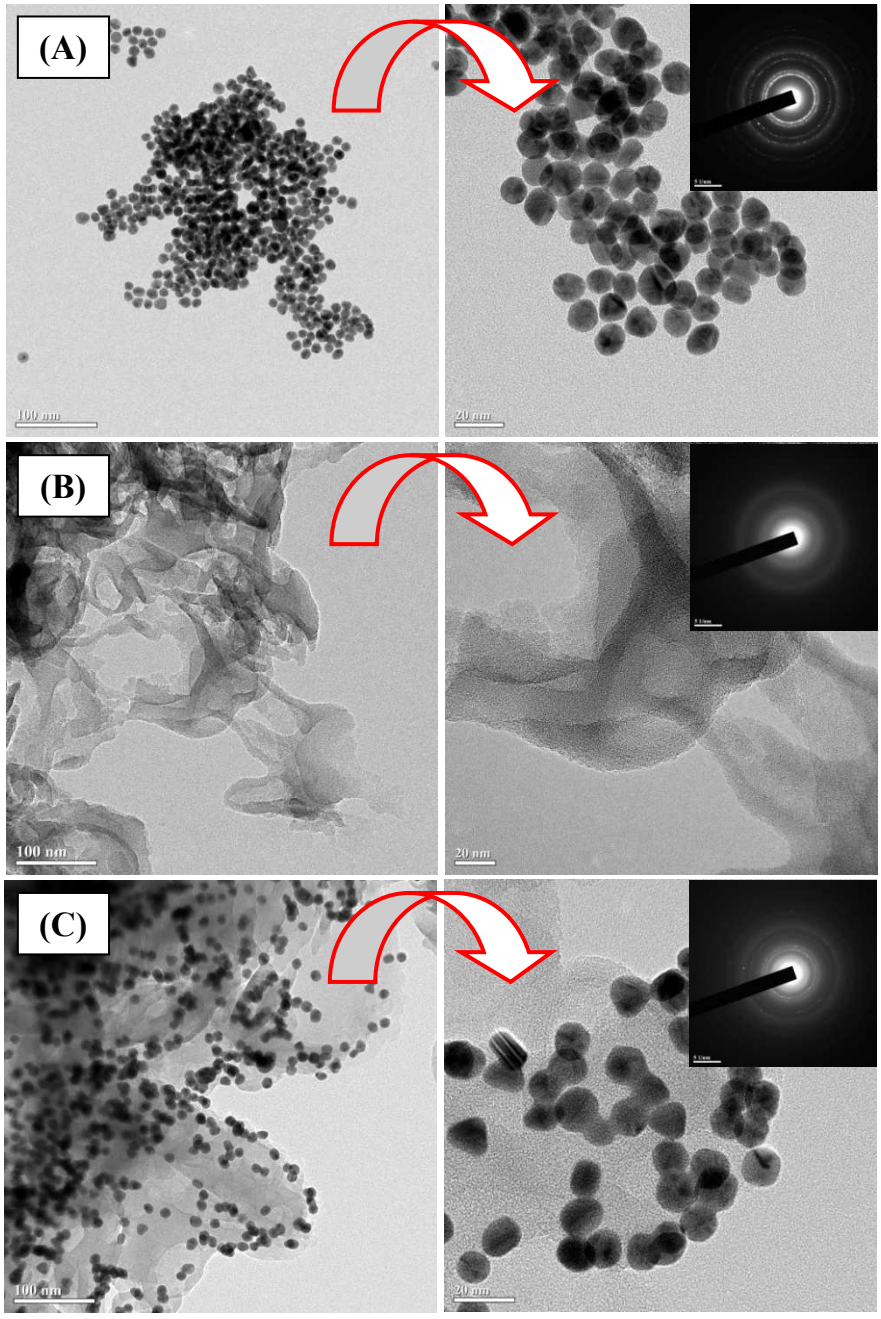

Figure 2(A to C)

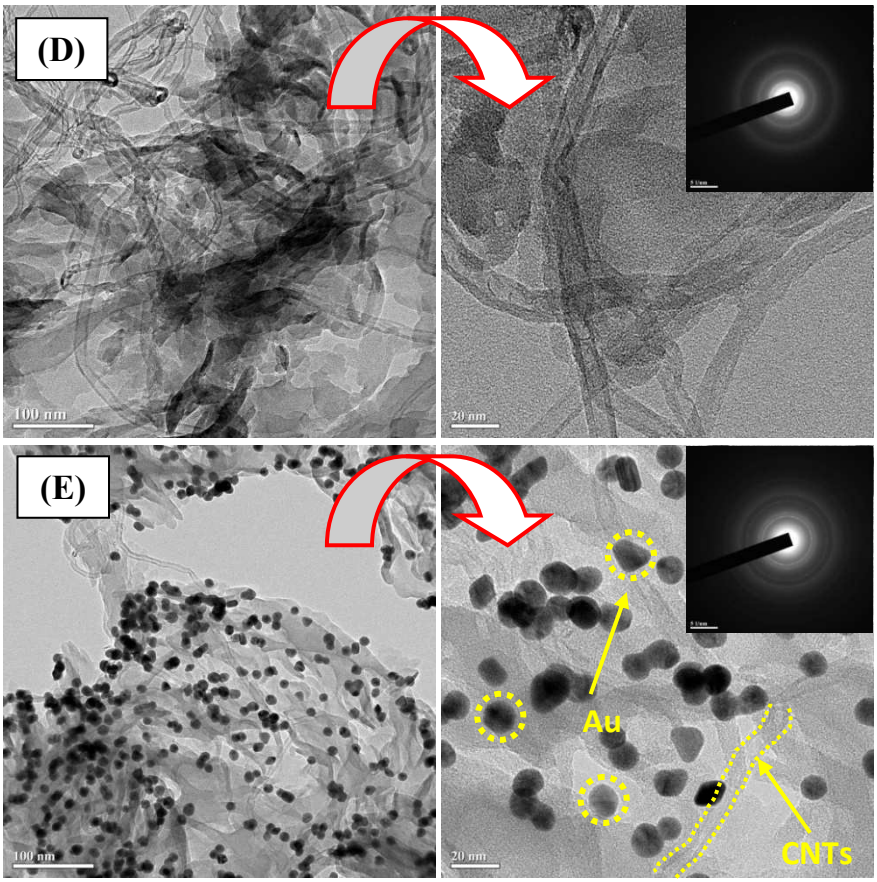

Figure 2(D and E)

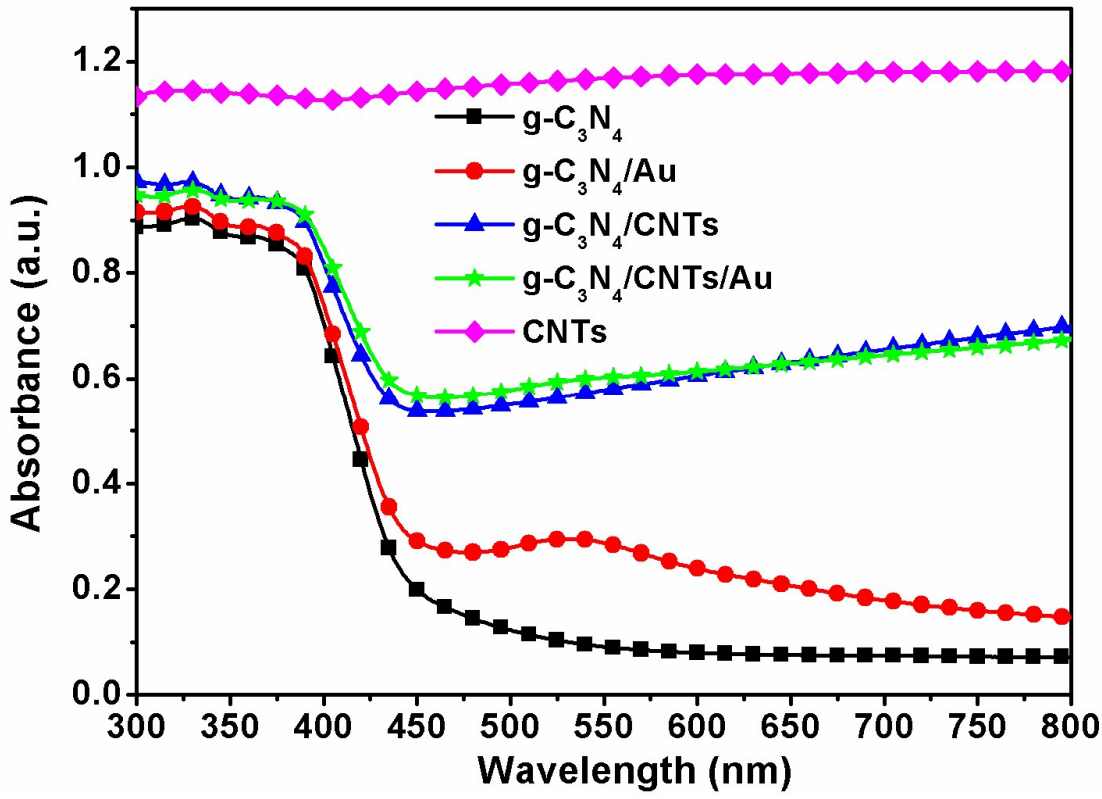

Figure 3

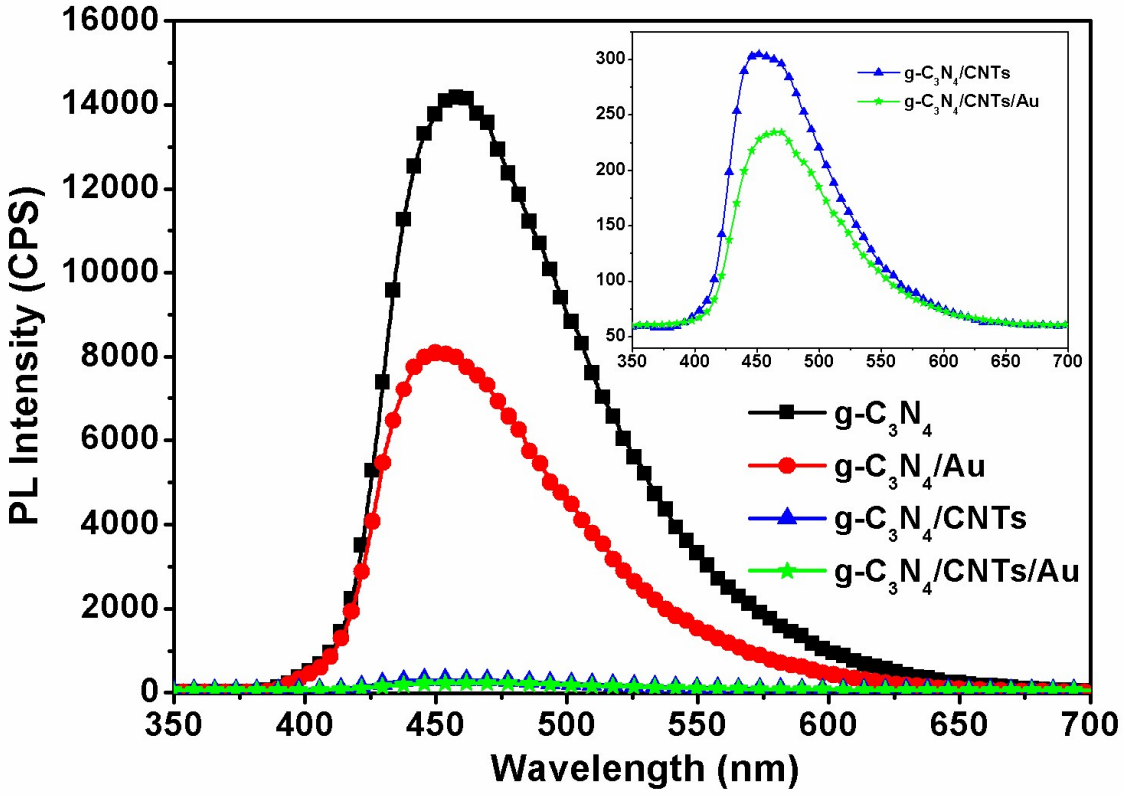

Figure 4

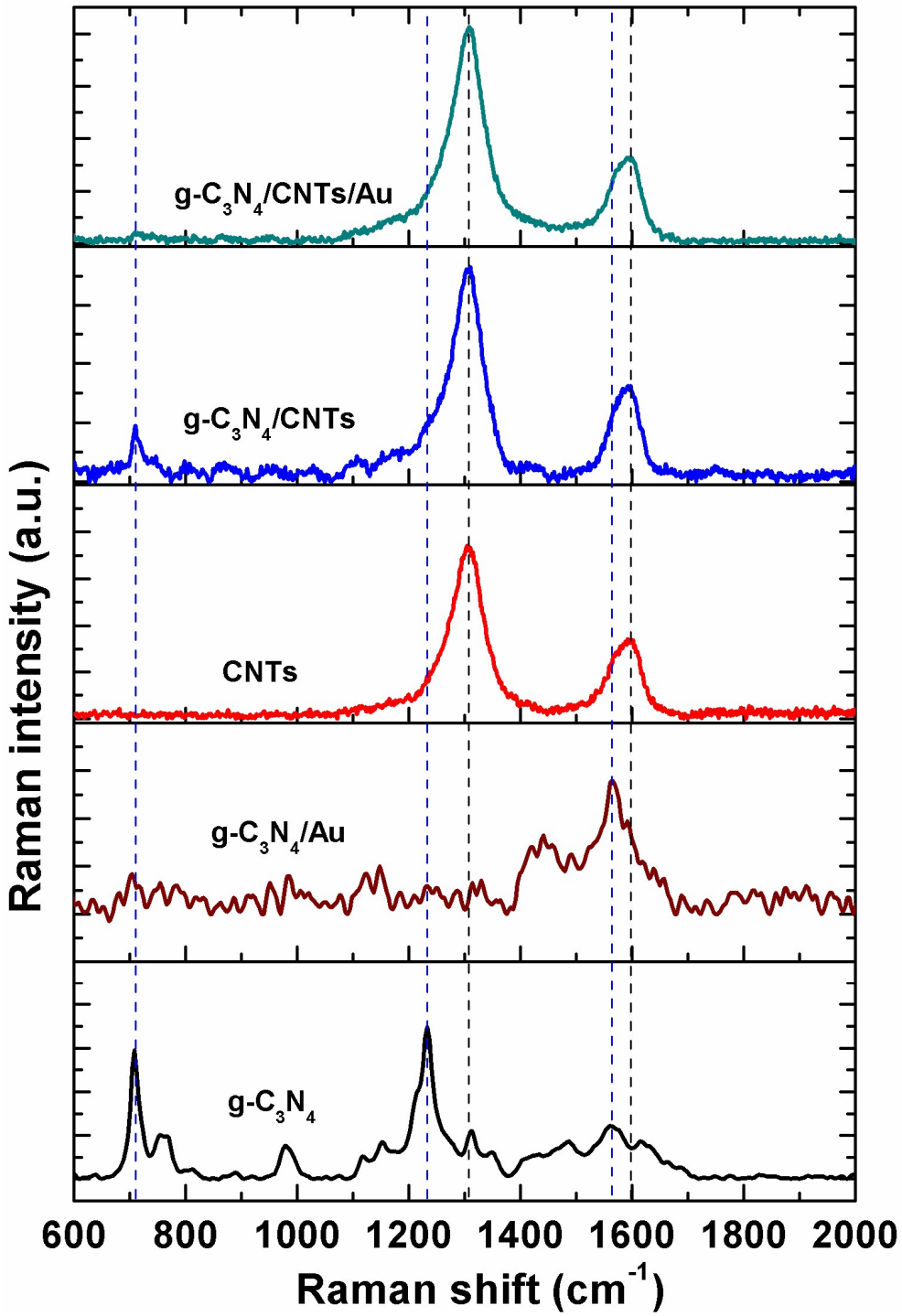

Figure 5

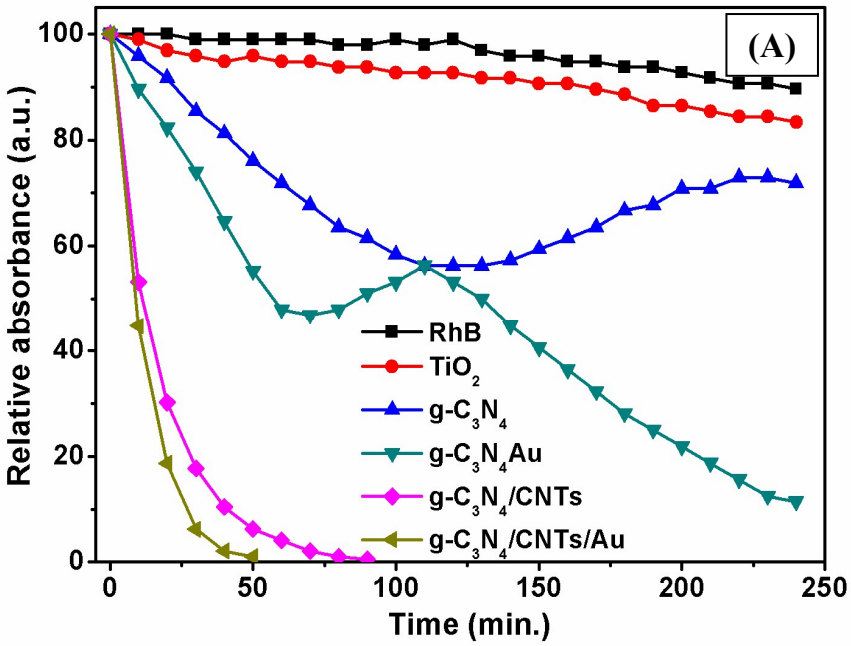

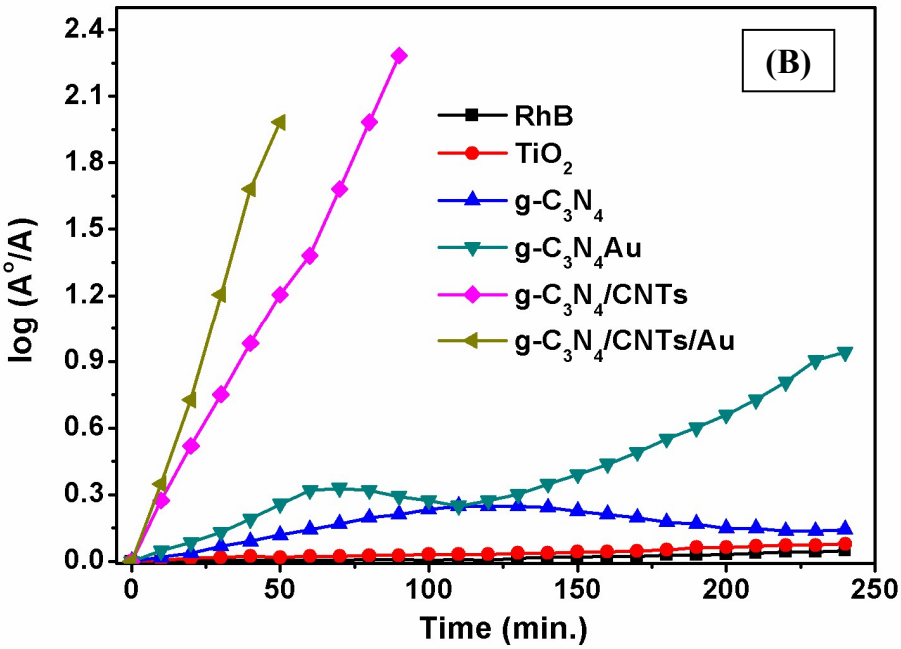

Figure 6(A and B)

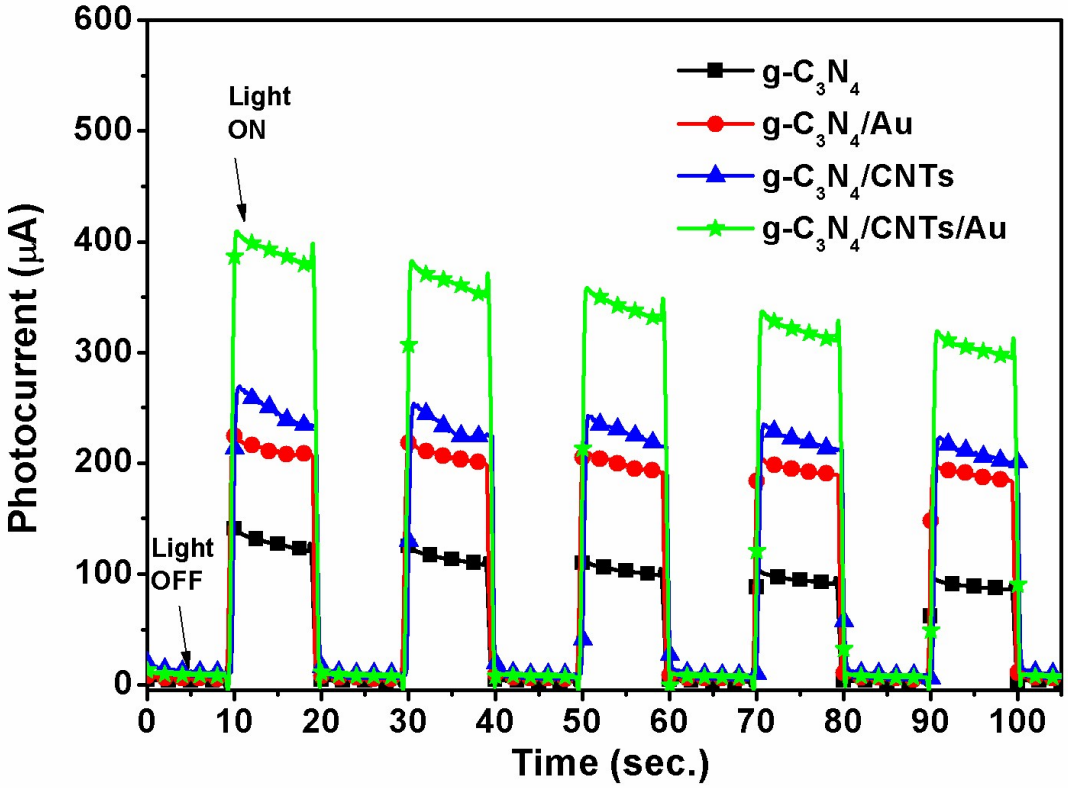

Figure 7

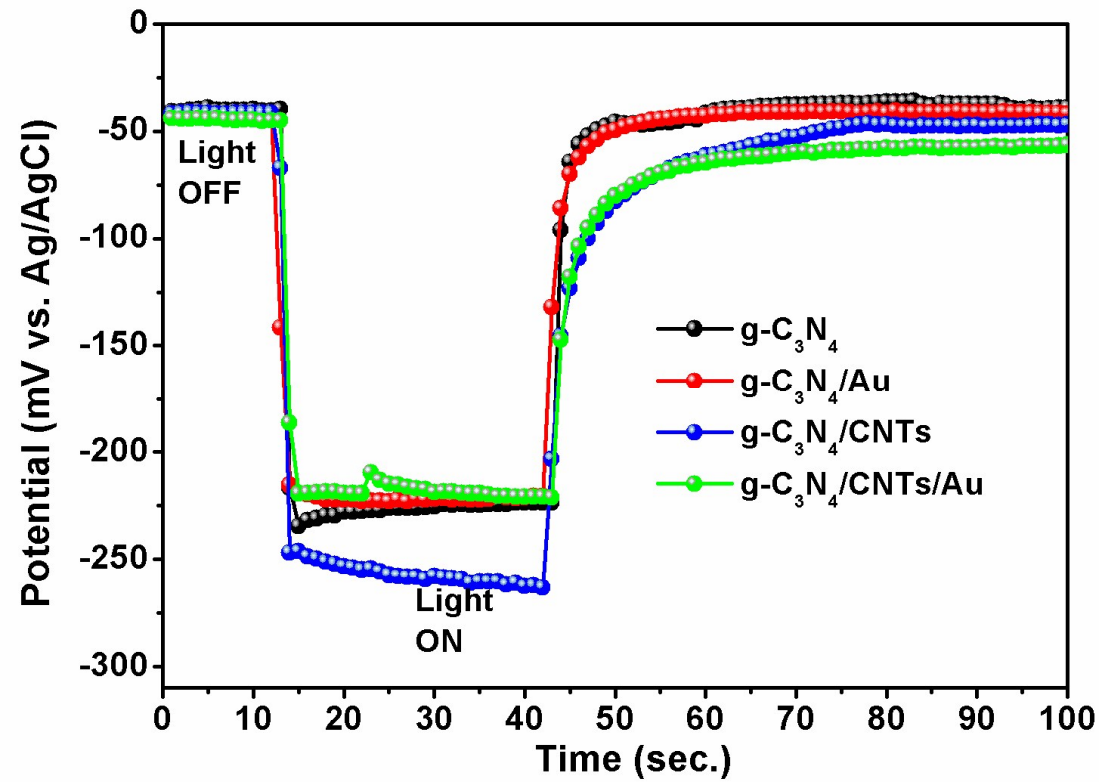

Figure 8

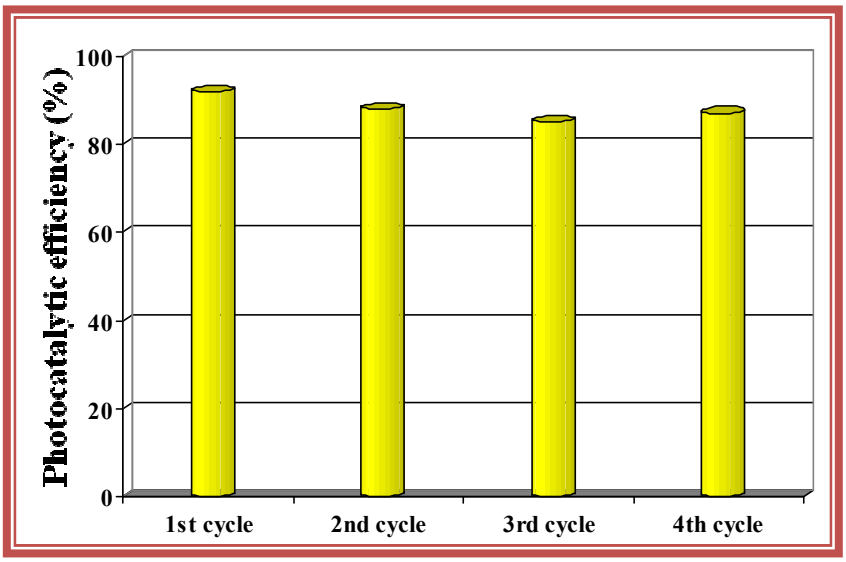

Figure 9

Sample details	Kinetic rate constant (K x 10^{-3}) min^{-1} Rhodamine B	TOC of Rhodamine B in μgCL^{-1}	Amount of Au in composite determined using ICP-AES (μg/kg)
RhB dye solution	0.19	18542	--
P25	0.29	15467	--
g-C_3N_4	0.46	14287	--
g-C3N_4/Au	3.28	6847	59777
g-C_3N_4/CNTs	27.79	2140	--
g-C_3N_4/CNTs/ /Au	41.10	1683	55056

Table 1

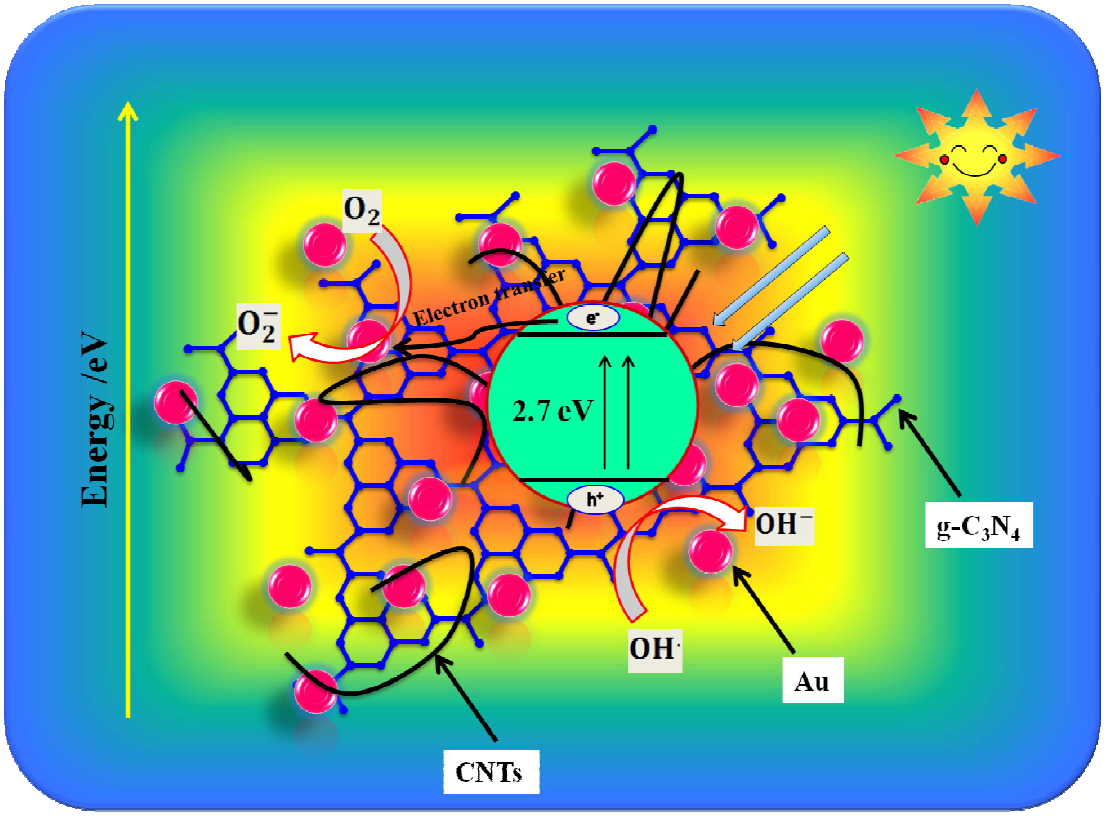

Schematic 1